npj | clean water

www.nature.com/npjcleanwater

ARTICLE OPEN

Check for updates

MOF-derived C, N-In_2O_3 with $GdFeO_3$ Z-scheme heterostructure for the photocatalytic removal of tetracycline

Karunamoorthy Saravanakumar[1], Govindan Jagan[1], Jongho Lee[2] and Chang Min Park[1]✉

Metal oxides derived from metal–organic frameworks have received considerable attention for water treatment. Herein, MIL-68 (In)–derived rod-like carbon (C) and nitrogen (N) codoped In_2O_3–modified $GdFeO_3$ (CN–InO/GdF) Z-scheme heterostructures were rationally constructed through simple pyrolysis and a wet-chemical route. The synthesized CN–InO/GdF catalysts were characterized using several physicochemical techniques. Moreover, the obtained CN–InO/GdF exhibited excellent photocatalytic performance toward tetracycline (TC) degradation. Impressively, the optimized CN–InO/GdF-3 heterostructure catalyst displayed a boosted TC removal efficiency of 99.06% within 60 min of irradiation, which was 7.1 and 9.7 times higher than those of bare CN–InO and $GdFeO_3$, respectively. The remarkably enhanced photoactivity of CN–InO/GdF was principally attributed to the synergistically combined interfaces hindering the recombination of photoinduced carriers, and the maintained redox capacity *via* Z-scheme spatial charge transfer. Finally, the tentative degradation mechanism was determined on the basis of density functional theory calculations and intermediates analysis. This work elucidated the design of highly efficient catalysts for various applications.

npj Clean Water (2023)6:72 ; https://doi.org/10.1038/s41545-023-00288-0

INTRODUCTION

Pharmaceutical antibiotics, originating from therapeutic medicine and feed supplements for livestock, are prevalent emerging pollutants in natural water[1]. Particularly, tetracycline (TC) is a widely used antibiotic in the prevention and treatment of bacterial infections, such as those by certain anaerobes[2]. According to statistics, TC ranks as the second most used antibiotic, accounting for nearly a third of total antibiotic consumption and production. Unfortunately, the ensuing misuse of TC and incomplete metabolic transformations can lead to severe impacts on ecological systems, and the residues of TC may exist in various types of water bodies (*e.g.*, in surface soil at <1.0–12.0 mg/kg)[3]. In aquatic environments, TC and its derivatives are very difficult to degrade, and they induce the spread of antibiotic-resistant genes[4,5]. Thus, effective and feasible methods for the quick degradation of antibiotics in wastewater must be identified[6]. Currently, several techniques are used to treat water pollutants[7,8]. However, conventional methods are expensive and form undesired secondary contaminants when dispersed into the environment, which necessitates further treatment[9].

Photocatalysis is an eco-friendly green approach to environmental remediation. At present, indium-based materials have attracted great interest in the catalytic field because of their stable physiochemical characteristics. Notably, indium oxide (In_2O_3) possesses a narrow energy gap of ~2.8 eV, in addition to exhibiting suitable photo redox ability and excellent thermodynamic stability, which are promising for degrading persistent organic pollutants from wastewater[10,11]. In this regard, Pawar et al. used the biogenic reflux method to fabricate an In_2O_3 nanocapsule for the degradation of crystal violet, which removed almost 90% of the pollutant in 3 h[12]. Meanwhile, Dai et al. synthesized In_2O_3 by calcinating $In(OH)_3$, which could be used for the decontamination of the sulfan blue dye[13]. Furthermore, phase pure In_2O_3 exhibits low catalytic efficiency and does not meet relevant expectations.

Metal–organic frameworks (MOFs) are a class of metal nodes and organic ligands connecting network frameworks, and they have emerged as well-regarded candidates in the field of sensing, adsorption, and catalysis[14,15]. However, the weak conductivity and poor thermal and water stability of MOFs hinder their practical application in water treatment. Fortunately, MOFs are ideal templates/precursors for the preparation of functional materials because of their adjustable composition, high metal content, and large surface area[16]. Thus, MOF-derived catalysts not only retain their porous structure but also possess ordered channels for the release of intermediates and transport of target pollutants[17]. Meanwhile, during high-temperature pyrolysis, organic linkers in MOFs can form carbon matrices and heteroatoms into their corresponding catalysts[18]. More importantly, in-situ heteroatom doping could facilitate the charge transfer rate and promote further defects, enabling the proliferation of populous reaction sites in photocatalysis[19]. Numerous MOF-derived photocatalysts have been synthesized and have exhibited remarkable photocatalytic performance. For instance, Sun et al. fabricated N, S–C/In_2O_3 hollow rods by adopting MIL-68 (In) as a template, with 1,2-benziothiazolin-3-one as the modulator for the source of S[11]. The synthesized N,S-C/In_2O_3 exhibited excellent activity for the photocatalytic oxidative hydroxylation of arylboronic acid and easy recovery. Meanwhile, the MIL-68 (In)–derived C/HT-In_2O_3/$ZnIn_2S_4$ heterostructure prepared by Zhang et al. greatly improved photocatalytic hydrogen generation *via* In–N–In sites[20]. Unfortunately, MOF-derived In_2O_3 possesses several limitations: the sluggish transfer of electrons, the rapid recombination of electron–hole pairs, and the reactive sites less exposed to light irradiation[21]. Consequently, effective photocatalyst systems with improved carrier separation for wastewater treatment must be designed.

Heterojunction construction, particularly the Z-scheme heterostructure, is an efficient pathway in improving carrier separation, while retaining redox ability[22,23]. According to the Z-scheme

[1]Department of Environmental Engineering, Kyungpook National University, 80 Daehak-ro, Buk-gu, Daegu 41566, Republic of Korea. [2]Department of Civil Engineering, University of British Columbia, Vancouver, BC V6T 1Z4, Canada. ✉email: cmpark@knu.ac.kr

structure, two semiconductors with staggered-band alignments can be connected by a reductive semiconductor with more negative conduction band (CB) potential and an oxidative semiconductor with more positive valence band (VB) potential[24]. In this regard, perovskite metal oxides have become one of the leading photocatalysts because of their unique structural features and high thermal and chemical stability[25,26]. Notably, gadolinium ferrite ($GdFeO_3$), a rare-earth orthoferrite with a narrow band gap (1.9–2.2 eV) and robust crystallographic properties, has been utilized in various applications including sensors[27], energy storage[28], and photocatalysis[29,30]. Furthermore, $GdFeO_3$ possesses a sufficient amount of positive VB potential to produce hydroxyl radicals (•OH), suggesting that $GdFeO_3$ could be used to build a Z-scheme with MOF-derived In_2O_3.

Inspired by the aforementioned strategies and concepts, we prepared MIL-68 (In)–derived CN–InO-microrod–modified $GdFeO_3$ Z-scheme heterostructure using the facile wet-chemical method. The synthesized CN–InO/GdF nanocomposites exhibited superior photocatalytic activity in eliminating TC. The boosted photocatalytic activity was attributed to the in-situ formation of C and N in rod-like In_2O_3 and the synergistic interaction between $GdFeO_3$ and CN–InO. Crucial environmental factors, such as the catalyst dosage, initial TC concentration, coexisting ions, and initial pH value on TC removal, were investigated. More importantly, the plausibility of the photocatalytic Z-scheme mechanism and toxicity assessments of the formed intermediates were also determined for TC degradation.

RESULTS AND DISCUSSION

Phase structure, chemical state, and morphology characteristics

The crystal phases of the as-prepared samples were identified using X-ray diffraction (XRD). The characteristic diffraction peaks of MIL-68 (In) were well matched with the simulated data for a single crystal, confirming the excellent crystallinity of the as-synthesized MIL-68 (In) (Supplementary Fig. 1). As presented in Fig. 1, three different temperature-controlled CN–InO samples were indexed with body-centered cubic In_2O_3 (JCPDS card # 06-0416). The major peaks at about 21.6°, 30.6°, 33.1°, 35.6°, 45.7°, 51.0°, and 60.7° were assigned to the (211), (222), (321), (400), (431), (440), and (622) diffraction planes, respectively[31]. Moreover, some of the characteristic peaks of CN–InO increased after the annealing temperature of 450°C. For S–In_2O_3 (Supplementary Fig. 2), the diffraction signals were in accordance with the standard cubic phase of In_2O_3 (JCPDS card # 06-0416). Meanwhile, pristine

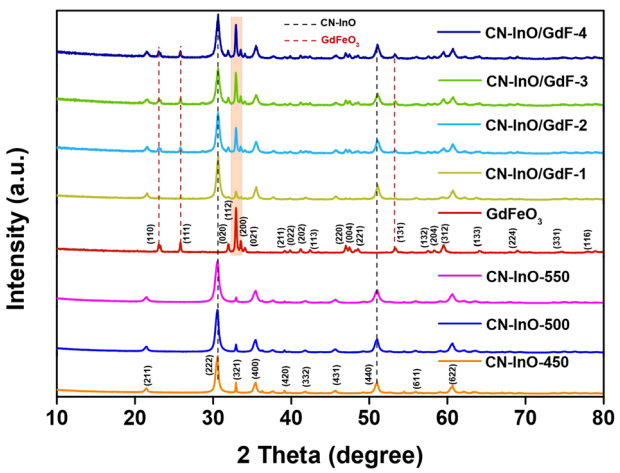

Fig. 1 XRD patterns. Comparison of XRD patterns of the as-prepared catalysts.

$GdFeO_3$ exhibited several peaks located at 23.1°, 25.8°, 32.8°, 46.9°, 53.2°, and 59.5°, which matched well with the (110), (111), (112), (220), (131), and (312) lattice planes of the orthorhombic crystal system of $GdFeO_3$ (JCPDS card # 47-0067), respectively[29]. After hybridizing CN–InO with $GdFeO_3$, the characteristic peaks of CN–InO and $GdFeO_3$ in the CN–InO/GdF nanocomposites were apparent, and no other distinct peaks existed. As the dosage of $GdFeO_3$ increased, the intensity of the diffraction peaks of CN–InO gradually weakened, and the peaks of $GdFeO_3$ gradually strengthened, verifying the successful formation of CN–InO/GdF heterostructures with higher crystallinity.

Fourier transform infrared (FTIR) spectroscopy was used to elaborate on the functional groups of the as-prepared samples. As presented in Supplementary Fig. 3, MIL-68 (In) showed prominent peaks in the range between 1380 and 1700 cm^{-1}, which could be ascribed to the stretching vibrations of the carboxylate group, whereas the bands at 550 and 770 cm^{-1} belonged to the vibration bonds of O–In–O[32]. The infrared spectrum of CN–InO was similar to that of S–In_2O_3, and the bands at ~562 and 596 cm^{-1} were assigned to the typical bending vibration of In–O and O–In–O bonds. For bare $GdFeO_3$, the band at ~418 cm^{-1} was attributed to the stretching mode of octahedral Fe–O (FeO_6) in the perovskite structure, and another peak found at 543 cm^{-1} was associated with Gd–O symmetric stretching vibration[28]. As expected, the spectra of the CN–InO/GdF composite showed the characteristic peaks of both CN–InO and $GdFeO_3$, proving the successful fabrication of the CN–InO/GdF.

The chemical composition on the surface and oxidation states of CN–InO, $GdFeO_3$, and CN–InO/GdF were investigated through X-ray photoelectron spectroscopy (XPS) analysis, as displayed in Fig. 2. The XPS survey spectra (Fig. 2a) suggests that C, N, In, O, Gd, and Fe elements are detectable in CN–InO/GdF, which further lends credence to the formation of the CN–InO/GdF heterojunction. The XPS spectrum of In 3d (Fig. 2b) can be divided into two distinct peaks at 451.72 and 444.17 eV, ascribed to In $3d_{3/2}$ and In $3d_{5/2}$ of In^{3+} ions for CN–InO, respectively. In comparison, In $3d_{3/2}$ and In $3d_{5/2}$ binding energies of CN–InO/GdF were red shifted to 451.3 and 443.7 eV. The decrease of binding energies results in the gaining electrons from adjacent $GdFeO_3$ and creates a unique electron cloud density on the CN–InO/GdF nanocomposite[33,34]. The XPS spectrum of O 1 s (Fig. 2c) displayed three peaks at 531.7, 530.6, and 529.5 eV, which were related to chemisorbed oxygen species (O–H and/or –OH), oxygen vacancies, and metal-bonded lattice oxygen, respectively. Similarly, the neat $GdFeO_3$ also displayed three peaks of O 1 s at 531.6, 530.5, and 529.2 eV. After CN–InO/GdF heterojunctions formation, the slight shifts occurred in the inner peaks, which leads to the electron exchange pathways in between the interface of CN–InO and $GdFeO_3$[11,35]. As shown in Fig. 2d, the C 1 s spectra of CN–InO exhibited three major peaks at 288.1, 285.4, and 284.3 eV, which were assigned to O–C=O, O–C/C–N, and C=C/C–C, respectively[36,37]. For CN–InO, its N 1 s spectra (Fig. 2e) could be deconvoluted into three peaks at 403.5, 400.0, and 398.2 eV, attributable to N=O, C=N (tertiary N), and C–N/C=N, respectively[38]. Meanwhile in the formation of CN–InO/GdF, the peaks were directed to the negative binding energies with distinct positions around 284.9, 285.1, and 287.7 eV for C 1 s and 397.7, 399.6, and 403.1 eV intended to N 1 s, respectively. In the high-resolution Gd 3d spectra (Fig. 2f), the two major peaks at 1219.1 and 1186.7 eV belonged to Gd $3d_{3/2}$ and Gd $3d_{5/2}$, respectively, and the binding energies of 1225.3 and 1192.7 eV corresponded to the satellite peaks. Apparently in CN–InO/GdF binary nanocomposite, the Gd $3d_{3/2}$ and Gd $3d_{5/2}$ peaks tend to blue shift towards higher binding energy levels, thus donating electrons to the nearby CN–InO heterojunction. Figure 2g shows the core-level XPS spectra of Fe 2p states fitted into two prominent peaks at 724.5 and 710.9 eV, which respectively corresponded to the Fe $2p_{1/2}$ and Fe $2p_{3/2}$ spin orbits of Fe^{3+} with a spin energy separation of 13.6 eV in $GdFeO_3$ and two

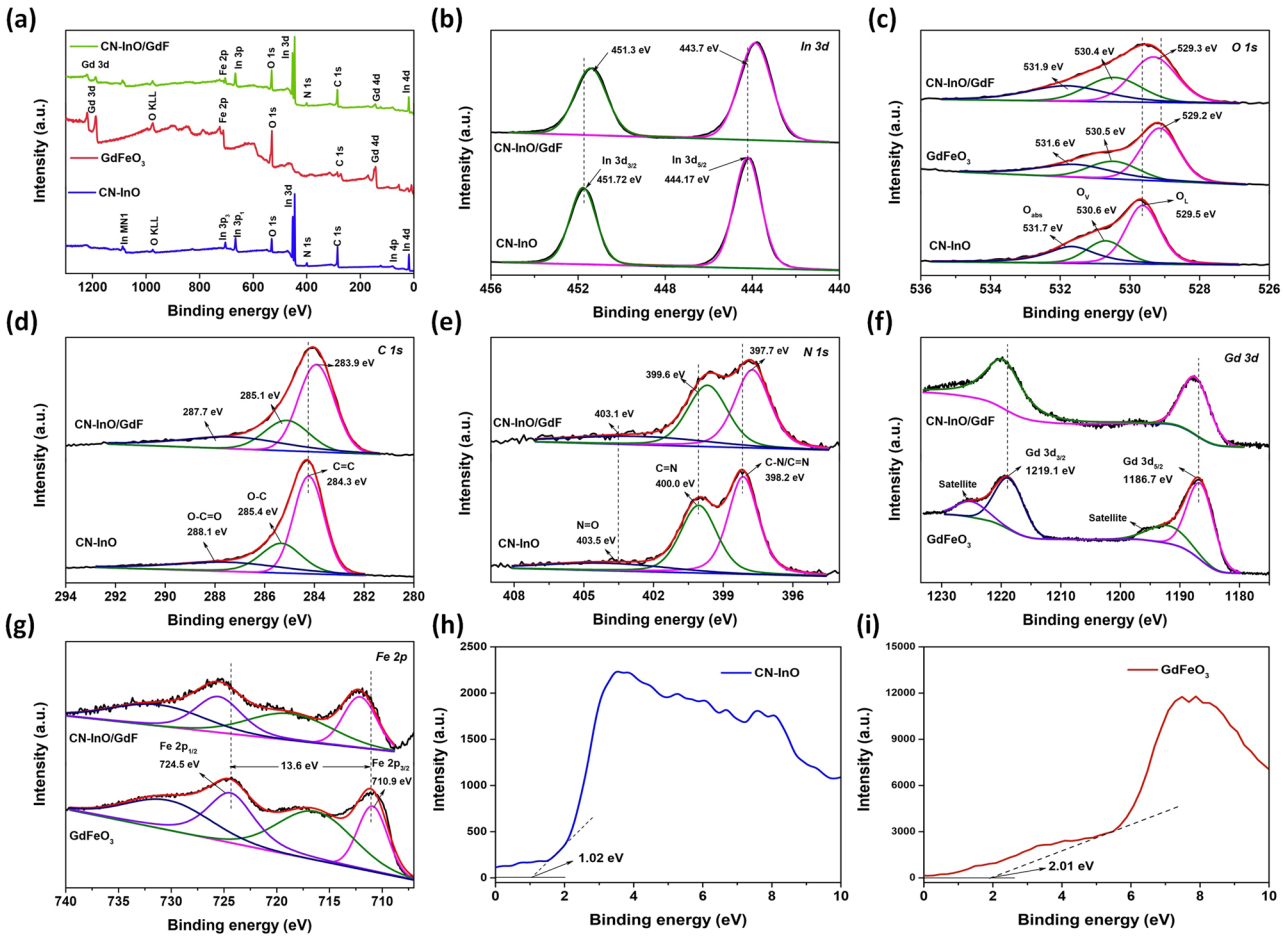

Fig. 2 XPS spectra of CN–InO, $GdFeO_3$, and CN–InO/GdF. a Survey spectrum.; high-resolution spectra of **b** In 3d, **c** O 1 s, **d** C 1 s, **e** N 1 s, **f** Gd 2d, **g** Fe 2p; and VB-XPS curves of **h** CN–InO and **i** $GdFeO_3$.

satellite peaks at 731.5 and 716.3 eV. Clearly, the Fe $2p_{1/2}$ and Fe $2p_{3/2}$ peaks were slightly shifted to higher binding energies for CN–InO/GdF, indicating that the electron cloud density was reduced after the heterostructure formation[29,39].

The textural properties of the as-synthesized catalysts were measured using the Brunauer–Emmett–Teller (BET) technique, as depicted in Supplementary Fig. 4. According to BET classification, all samples were confirmed as type-IV adsorption isotherms with a hysteresis loop ($P/P_0 = 0.6–1.0$), which indicated the presence of a mesoporous structure. The calculated surface area and Barrett–Joyner–Halenda (BJH) pore distributions of all samples are listed in Supplementary Table 1. The BET surface areas of CN–InO, $GdFeO_3$, CN–InO/GdF, and S–In_2O_3 were 112.2, 3.070, 66.80, and 38.93 m^2/g, corresponding to the BJH pore volumes of 0.1661, 0.0092, 0.1063, and 1814 cm^3/g, respectively. Moreover, the specific surface area of the S-In_2O_3 material was only 38.93 m^2/g, whereas that of CN–InO was 112.2 m^2/g. After the coupling of CN–InO and $GdFeO_3$, the BET surface area of the CN–InO/GdF nanocomposite decreased, which may be attributable to the aggregation and/or obstruction of the mesopores of CN–InO by $GdFeO_3$ during synthesis[40,41]. This revealed that the CN–InO/GdF nanocomposite possesses an abundance of active sites and was thus favorable for photocatalytic efficiency.

The morphological analysis of pure and CN–InO/GFO nanocomposites was conducted using field emission scanning electron microscopy (FESEM) and high-resolution transmission electron microscopy (HRTEM) techniques. As displayed in Supplementary Fig. 5a, MIL-68 (In) exhibited a solid rod-like structure with smooth surfaces and the diameters of prisms ranged from 0.5 to 1 µm. After annealing under an O_2 atmosphere (Supplementary Fig. 5b), hexagonal rods (namely, S-In_2O_3) appeared on a hollow-structured rough surface, and their diameters were ~1 µm. Subsequently, CN–InO was also pretreated in the presence of an N_2 medium (Fig. 3a), wherein the rough surfaces were covered with C and a considerable amount of N atoms (~1 µm in diameter). From Fig. 3d, the resulting HRTEM images of the CN–InO sample emerged with a homogenous surface, which resulted in a superior catalytic active site. As depicted in Fig. 3b and e, $GdFeO_3$ was coordinated as porous microsphere-like structures with an average size of 1.0–1.2 µm and with pores 50–100 nm in diameter. In the nanocomposite formation (Fig. 3c and f), the $GdFeO_3$ microspheres were gently bound with the surfaces of CN–InO rods, thus resulting in greater migration of charge carriers within the interfaces of the CN–InO/GdF heterojunction. From the HRTEM images (Fig. 3g, h), the lattice fringe distances were found to be approximately 0.272 and 0.292 nm, ascribed to the interplanar spacing of the (1 1 2) crystal planes of GdF and (2 2 2) CN–InO, respectively. The inset in Fig. 3i represents the selected area diffraction pattern with rings corresponding to (2 2 2), (1 1 2), (4 1 3), and (3 1 2) planes from the surfaces of the CN–InO/GdF heterostructure. As shown in Fig. 3j and Supplementary Fig. 6a–c, the energy-dispersive X-ray analysis (EDAX) mapping and spectrum further signified the spreading of C, N, In, Gd, Fe, and O elements over the formation of CN–InO/GdF. In addition, the elemental distributions were indicated in cyan, magenta, green, yellow, orange, and red, respectively. Besides, the TEM and EDAX profiles evidently confirmed the successful regulation of the CN–InO/GdF heterojunction.

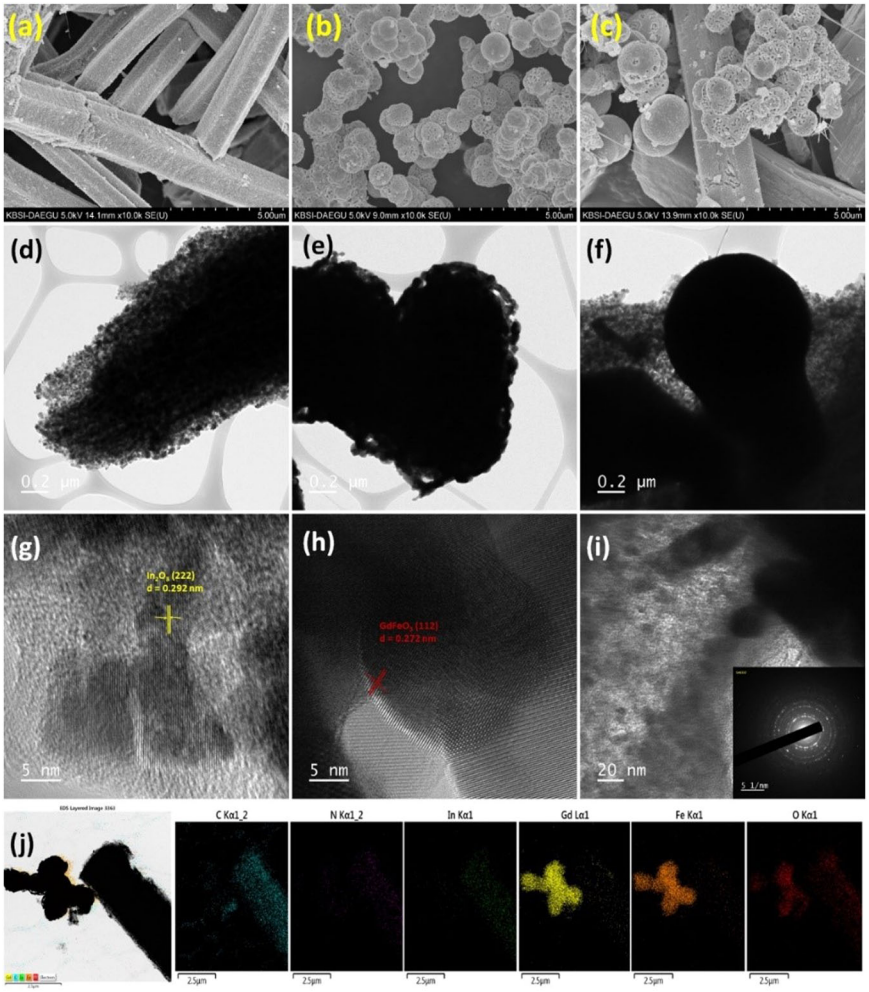

Fig. 3 Physicochemical characterization. FESEM images of **a** CN–InO, **b** $GdFeO_3$, **c** CN–InO/GdF. HRTEM images of **d**, **g** CN–InO, **e**, **h** $GdFeO_3$, and **f**, **i** CN–InO/GdF with corresponding SAED pattern (inset). **j** EDAX elemental (C, N, In, Gd, Fe, and O) mapping of the CN–InO/GdF nanocomposite.

Photophysical characteristics of CN–InO/GdF

The light-harvesting ability and bandgap of CN–InO, $GdFeO_3$, and CN–InO/GdF heterostructures were investigated *via* UV–Vis diffuse reflectance spectroscopy (DRS) analysis. As presented in Fig. 4a, MIL-68 (In) possessed an optical absorption margin of ~420 nm. After pyrolysis, MIL-68 (In) was converted into CN–InO, and the absorption edge effectively expanded because of the presence of carbon. The perovskite $GdFeO_3$ showed a stronger light absorption edge close to 610 nm, which was due to the electron transfer transition of O 2p to the Fe 3d orbital[26,42]. Upon the incorporation of $GdFeO_3$ into CN–InO, the CN–InO/GdF heterostructures exhibited a slight redshift of the light absorbance, and a decrease in the absorbance range was observed with the additional $GdFeO_3$ content. This shift was probably due to the synergistic interaction and heterojunction formation between CN–InO and $GdFeO_3$. More explicitly, the optical bandgap energies of the as-prepared catalysts were determined using Tauc's method ($[\alpha h\nu]^2 = A[h\nu - E_g]$)[43,44]. According to the Tauc plot functions (Fig. 4b), the calculated bandgap values of MIL-68 (In), CN–InO, $GdFeO_3$, CN–InO/GdF-1, CN–InO/GdF-2, CN–InO/GdF-3, and CN–InO/GdF-4 were 2.91, 1.38, 2.05, 1.40, 1.43, 1.44, and 1.47 eV, respectively.

Steady-state photoluminescence (PL) spectra helped reveal the interfacial charge transfer and the separation efficiency of electron–hole pairs[8]. Figure 4c compares the PL spectra of pristine CN–InO and CN–InO/GdF nanocomposites at an excitation wavelength of 470 nm. The neat CN–InO exhibited the strongest emission band at ~510 nm, suggesting a rapid charge recombination in CN–InO. As expected, the PL peak intensity of the CN–InO/GdF composites significantly decreased, revealing efficient interfacial charge separation and migration. CN–InO/GdF-3 displayed the lowest PL intensity, which represented the enhancement in electron transfer and suppressed recombination through suitable band alignment. In addition, the time-resolve PL decay curves were fitted by an exponential factor and used to calculate the average fluorescence lifetime of the samples, as illustrated in Fig. 4d. The average decay lifetimes (τ_{avg}) of CN–InO and CN–InO/GdF-3 was found to be 0.368 and 0.263 ns, respectively. The shortened lifetime of the CN–InO/GdF-3 hybrid revealed that the heterojunction structure could accelerate the transfer of electrons on the surface of the catalyst, which positively affected the photocatalytic performance.

The charge–transport properties of the catalysts were further characterized through electrochemical impedance spectroscopy and transient photocurrent using a three-electrode system. The sizes of the Nyquist arc radii were in the following order: $GdFeO_3$ > CN–InO > CN–InO/GdF-1 > CN–InO/GdF-2 > CN–InO/GdF-4 > CN–InO/GdF-3. As shown in Fig. 4e, the CN–InO/GdF-3 catalyst exhibited the smallest arc radii among all samples, demonstrating its lowest interfacial charge transfer resistance and inhibiting charge recombination[45]. Meanwhile, the CN–InO/GdF-3 catalyst showed the highest photocurrent signals compared with the other catalysts, which implied that the photogenerated charge

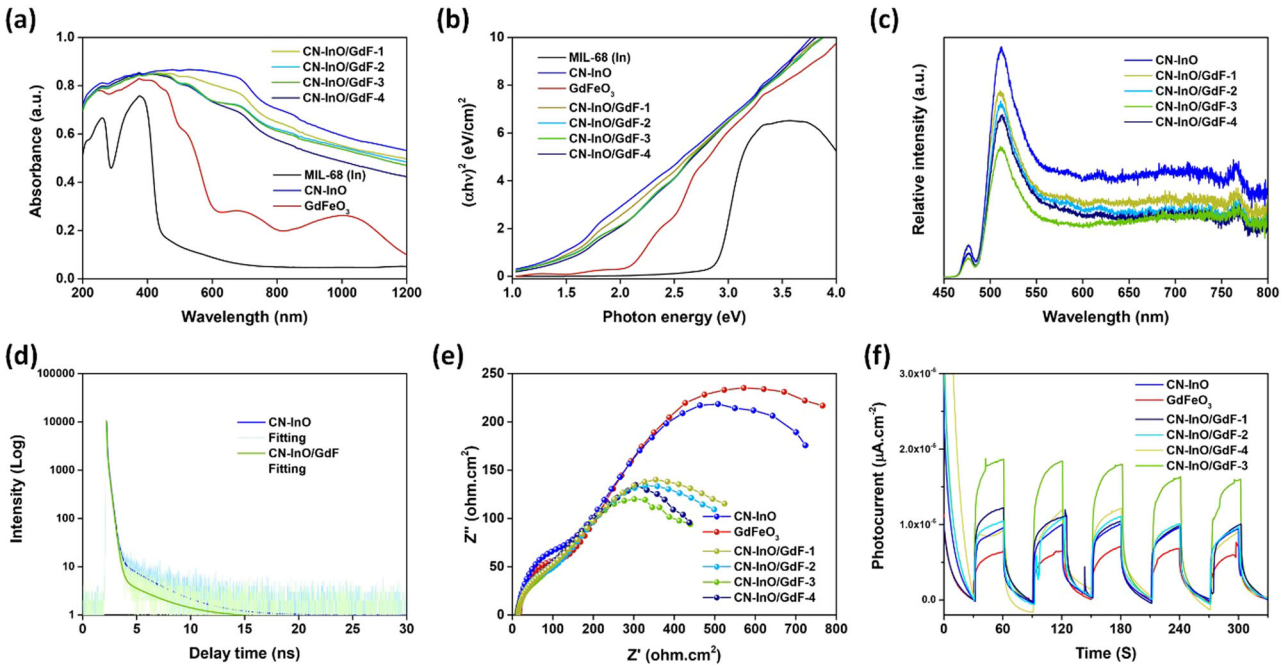

Fig. 4 Photophysical characterization. a UV–Vis DRS spectra. **b** Bandgap energy from the plots of $(\alpha hv)^2$ *vs*. *hv*. **c** PL spectra of the as-synthesized catalysts. **d** TR-PL spectra of CN–InO and CN–InO/GdF. **e** EIS spectra. **f** Transient photocurrent response spectrum of the as-synthesized catalysts.

separation of CN–InO/GdF-3 was improved effectively with prolonged lifetimes of the charge carriers. Therefore, all of these findings indicated that the strong interfacial interaction of $GdFeO_3$ and CN–InO could promote the production of charges and afford the separation of electron–hole pairs.

Photocatalytic evaluation of the CN–InO/GdF heterostructure

The photocatalytic capabilities of the as-prepared samples were investigated through the removal of TC under visible light irradiation (Fig. 5a). Only 26.9%, 41.4%, and 43.7% of TC were degraded after 60 min of light illumination using pure MIL-68 (In), $GdFeO_3$, and S-In_2O_3, respectively. Notably, the removal ability of the CN–InO samples increased with increasing sintering temperatures from 450°C to 500°C. This was attributed to the fact that the formed carbon and nitrogen acted as the electron transport media in CN–InO. When the annealing temperature increased from 500°C to 550°C, the decontamination rate of TC decreased from 48.4% to 32.6%, which may be attributable to the higher temperature of the calcination process leading to the formation of greater carbon content in the CN–InO sample and the loss of active sites[20]. Subsequently, 500 °C was chosen as the optimum temperature for the CN–InO synthesis. However, no TC photodegradation efficiency was observed by single components, attributed to the lower charge transfer and higher recombination of electron–hole pairs[43,46]. As expected, the TC degradation rate significantly improved when CN–InO formed heterostructures with $GdFeO_3$. The addition of $GdFeO_3$ into the CN–InO matrix could decrease the recombination of the charge carriers, thereby accelerating the degradation rate. Particularly, the CN–InO/GdF-3 catalyst showed a high photocatalytic performance, removing up to 99.06% of TC within 60 min. The enhanced activity of CN–InO/GdF-3 catalyst was due to a suitable band alignment, and stronger absorption of visible light for generating electron-hole pairs at the interfacial contact, as evident from the Tauc plot and photocurrent analysis. In contrast, too much $GdFeO_3$ content created structural distortion, which further affected the CN–InO active sites, suggesting that the proper mass ratios of $GdFeO_3$ are crucial for the effective decomposition of TC[36]. Under the same reaction conditions, the reaction rate constant (k) for the TC removal followed the trend of CN–InO/GdF-3 (0.0536/min) > CN–InO/GdF-4 (0.0231/min) > CN–InO/GdF-2 (0.0191/min) > CN–InO/GdF-1 (0.0102/min) > CN–InO (0.0076/min) > S-In_2O_3 (0.0057/min) > $GdFeO_3$ (0.0055/min) > MIL-68 (In) (0.0035/min), which well corresponded with analytical results shown in Fig. 4c–f. According to pseudo-first-order kinetic calculations (Supplementary Fig. 7 and Supplementary Table 2), the k value of CN–InO/GdF-3 ($k = 0.0536$/min) was approximately 15.3, 9.7, 7.1, 5.2, 2.8, and 2.3 times higher than those of MIL-68 (In), $GdFeO_3$, CN–InO, CN–InO/GdF-1, CN–InO/GdF-2, and CN–InO/GdF-4, respectively. Thus, the CN–InO/GdF-3 heterojunction catalyst exhibited superior photocatalytic activity toward TC degradation.

The impacts of catalyst dosage, initial pollutant concentration, initial pH, and coexisting ions on TC degradation were further estimated. With increasing CN–InO/GdF-3 catalyst loading (0.2 to 0.4 g L^{-1}), the TC removal rate considerably increased from 52.2% to 92.2% at 60 min (Fig. 5b). Further, the catalyst dosage increased from 0.4 to 0.6 g L^{-1}, and the degradation efficiency increased to 99.06% because of the more accessible active sites for the generation of reactive radicals. Figure 5c displays the effect of the initial concentration of TC (5–20 mg L^{-1}) on the photocatalytic reaction, with the other parameters being identical. The removal efficiency decreased sharply when the TC concentration further increased from 10 to 15 mg L^{-1}, and the decontamination rate of TC could still exceed 81%. In contrast, the gradually increasing TC concentration competed for engaging reaction sites on the CN–InO/GdF-3 surface, which diminished the degradation rate of TC[47]. Therefore, a catalyst dosage of 0.4 g L^{-1} and TC concentration of 10 mg L^{-1} were determined to be the suitable amounts for further photocatalytic reactions.

To identify the interfering ions on the TC removal process, the influence of common anions (Cl^-, NO_3^-, HCO_3^-, and SO_4^{2-}) was measured under visible light, and the results are depicted in Figure 5d. Therein, the addition of Cl^- and NO_3^- had little effect on TC degradation when compared with the control reaction. In the presence of HCO_3^-, the degradation of TC declined to 71.5%,

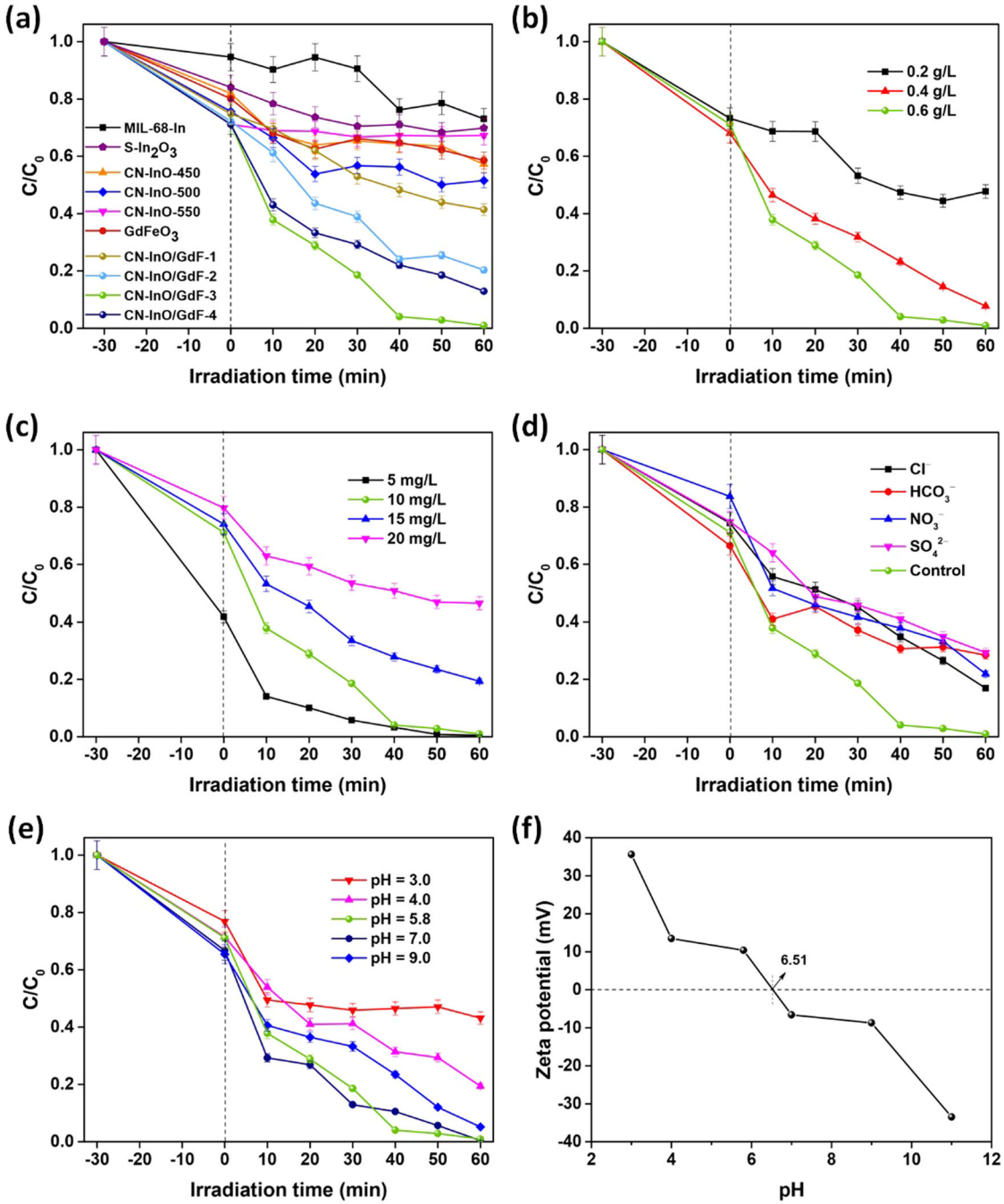

Fig. 5 Photocatalytic degradation of TC. Effects of **a** various synthesized catalysts, **b** catalyst dosage, **c** initial TC concentration, **d** coexisting ions, and **e** solution pH. **f** Zeta potential of CN–InO/GdF-3 catalyst as the function of pH value of the suspension. Reaction conditions: catalyst dose = 0.6 g L^{-1} (except for graph b), $[TC]_0$ = 10 mg L^{-1} (except for graph **c**), solution volume = 50 mL, pH = 5.8 (except for graph **e**), reaction time = 60 min, and temperature = 25 °C ± 2°C. The error bar represents the standard error.

which may be attributed to the fact that HCO_3^- acted as a strong scavenger of free radical species of $^{\bullet}OH$ and h^+[48]. Meanwhile, the addition of SO_4^{2-} displayed a remarkable inhibition effect, which was attributed to SO_4^{2-} also quenching reactive oxidative species (ROS).

Investigating the impact of pH is a robust parameter for studying the removal of TC as pH variations correlated with the formation of free radicals on catalyst surfaces. Fig. 5e suggests that the photocatalytic activity was enhanced when the pH was increased from 3 to 5.8, followed by a decrease at a pH of 9. Generally, TC is an amphoteric molecule with three unique electric charges: H_3TC^+ (pH < 3.3), H_2TC^0 (3.3 < pH < 7.7), and HTC^-/TC_2^- (7.7 < pH)[49]. Meanwhile, the point of zero charge (pH_{pzc}) of the CN–InO/GdF-3 catalyst (pH_{pzc} = 6.52) was measured through zeta potential analysis (Fig. 5f). In this case, the photocatalytic performance was weak at pH = 3. When the reaction occurs under acidic conditions, the catalyst should be positively charged in the solution. Because of electrostatic repulsion, the adsorption of TC molecules on the catalyst surfaces dropped, which not only led to a poor adsorption effect but also worsened the removal effect. However, the optimal degradation rate was obtained at the pH of 5–7, reaching ~99%. Upon further increasing the pH to 9,

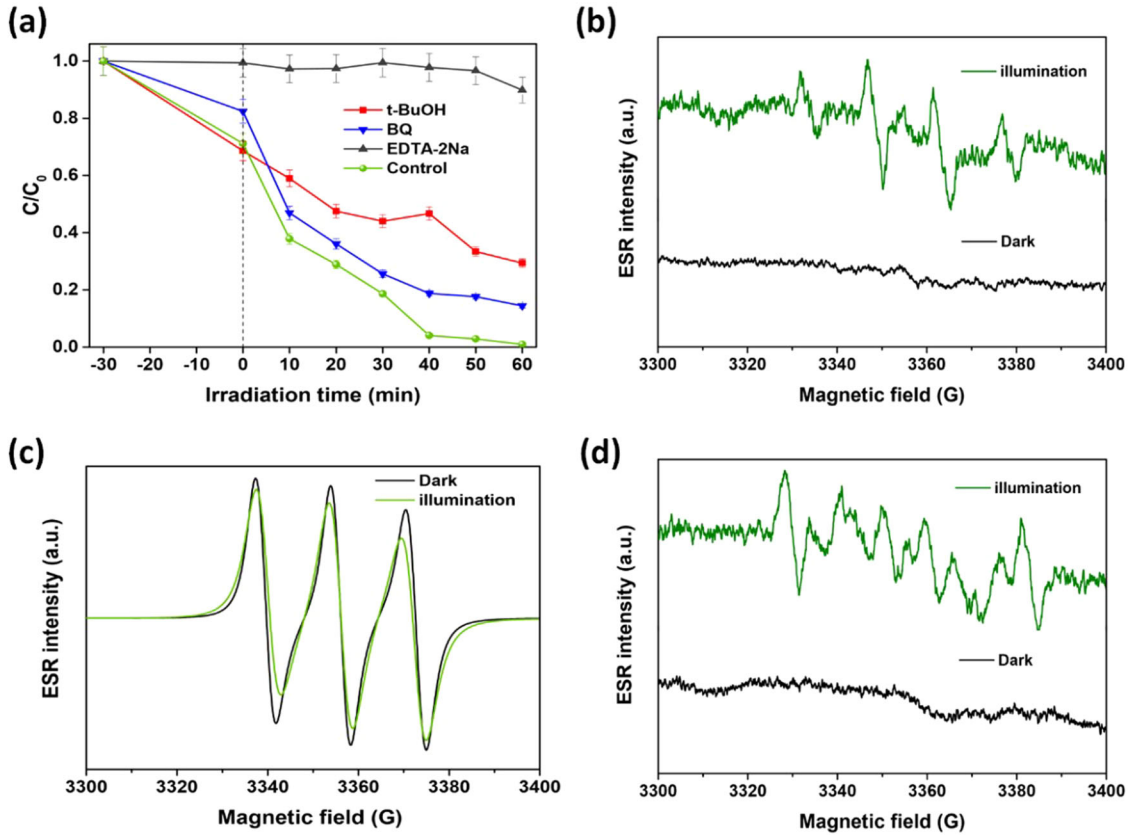

Fig. 6 Study on mechanism of CN–InO/GdF. a Radical sacrificial agent experiments during the photocatalytic degradation of TC. ESR spectra of **b** DMPO-$^{\bullet}$OH in H_2O, **c** TEMPO-h^+ in H_2O, and **d** DMPO-$^{\bullet}O_2^-$ in methanol media using CN–InO/GdF. Reaction conditions: catalyst dosage = 0.6 g L^{-1}, [TC] = 10 mg L^{-1}, pH = 5.8, solution volume = 50 mL, and temperature = 25 °C ± 2°C. The error bar represents the standard error.

the electrostatic repulsive forces slightly hindered the TC degradation.

The photostability of the catalyst was also investigated through recycling experiments. In Supplementary Fig. 8a, the CN–InO/GdF-3 heterostructure composite showed excellent stability of over 82.8% after four repeated uses, while continuing to retain its efficiency under visible light. Notably, the slight decreases in activity were primarily due to the ineluctable loss of the catalyst and the accumulation of intermediates on the active sites of the catalyst[50]. Furthermore, the phase and chemical structural properties of the used CN–InO/GdF-3 sample were characterized using XRD and FTIR. No obvious XRD peak intensity changes were observed for the used catalyst as compared with a fresh sample (Supplementary Fig. 8b). Meanwhile, the major functional group of the fresh and used catalysts remained almost unchanged (Supplementary Fig. 8c), indicating the excellent stability of the CN–InO/GdF-3 heterojunction in the photodegradation reaction.

Possible photocatalytic mechanisms, pathways, and toxicity assessments

Radical quenching tests were performed to verify the ROS and their influence on the TC degradation process. In this regard, ethylenediaminetetraacetic acid disodium (EDTA-2Na), tertiary butanol (t-BuOH), and benzoquinone (BQ) were used as scavengers of h^+, $^{\bullet}OH$, and $^{\bullet}O_2^-$, respectively[51]. As illustrated in Fig. 6a, the addition of BQ and t-BuOH to the photocatalytic process had no significant effect on the TC removal, implying that $^{\bullet}OH$ and $^{\bullet}O_2^-$ were secondary reactive species. Upon the addition of EDTA-2Na, almost no photodegradation was observed, which indicated that the photogenerated h^+ was the pivotal species for the decontamination of TC. Simultaneously, the formation of ROS was further elucidated by electron spin resonance (ESR) spectra using 2,2,6,6-tetramethylpiperidine-N-oxyl (TEMPO) and 5,5-dimethyl-1-pyrroline N-oxide (DMPO) as spin trap reagents. No noticeable ESR signals were detected in the dark conditions, whereas signals of DMPO–$^{\bullet}OH$ (Fig. 6b) and DMPO–$^{\bullet}O_2^-$ (Fig. 6d) were clearly detected upon light irradiation. In Fig. 6c, the intensity of the triple signals of TEMPO-h^+ was stronger than that of the light illumination because more h^+ were produced and separated by the CN–InO/GdF catalyst. These findings were consistent with the scavenging tests and scheme of charge transfer.

Based on the analyses and results, a possible photocatalytic charge transfer mechanism for the CN–InO/GdF heterojunction was proposed, as schematically described in Fig. 7. The energy gap values of pure $GdFeO_3$ and CN–InO computed using Tauc's plots were approximately 2.05 and 1.38 eV, respectively. From the VB ultraviolet photoelectron spectrum analysis (Fig. 2h, i), the VB potentials of CN–InO and $GdFeO_3$ were calculated as 1.02 and 2.01 eV *vs* normal hydrogen electrode (NHE), respectively. According to $E_{CB} = E_{VB} - E_g$, the CB edge was estimated to be −0.36 eV (*vs* NHE) for CN–InO and −0.04 eV (*vs* NHE) for $GdFeO_3$. Theoretically, the photocatalytic mechanism of CN–InO/GdF could form two feasible paths (traditional type-II mode or Z-scheme) for the charge transfer. Both CN–InO and $GdFeO_3$ could be excited under light illumination and produce electron–hole pairs at their CBs and VBs separately. In the type-II model, the photogenerated electrons in the CB of CN–InO would be transferred to the CB of $GdFeO_3$; synchronously, the produced hole in the VB of $GdFeO_3$ could migrate to the VB of CN–InO. Consequently, the photo-induced charge carriers would migrate, and the separation rate would be increased[46]. However, the agminated holes in the VB of

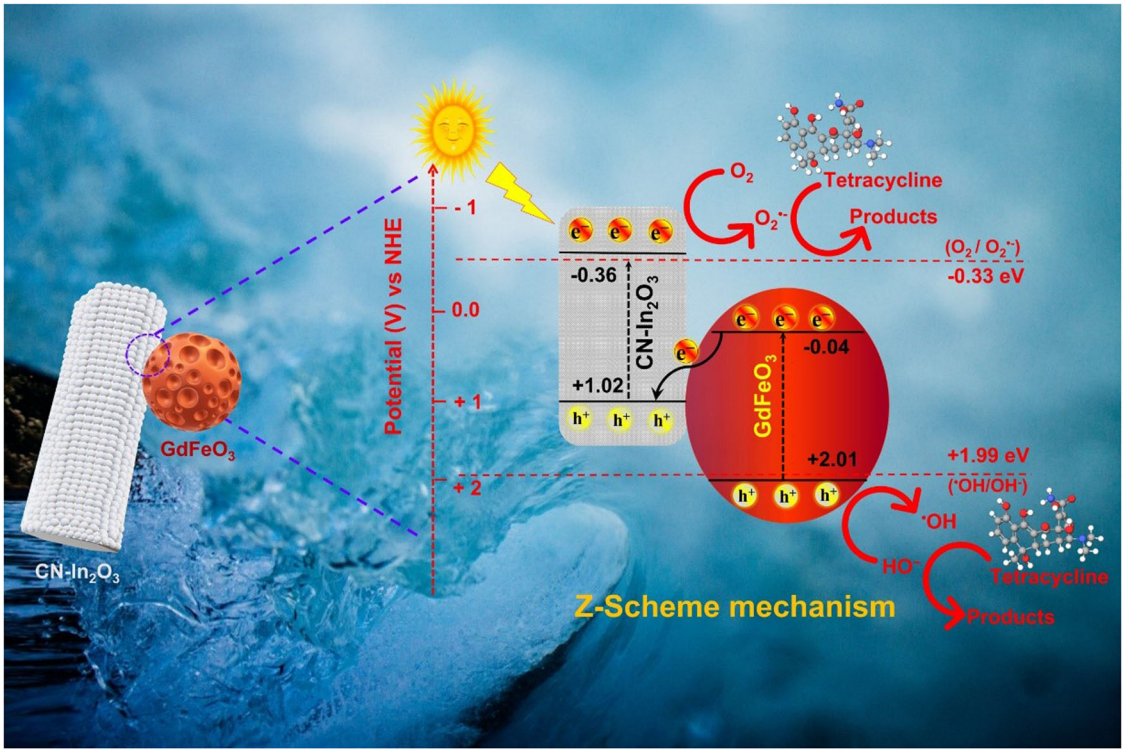

Fig. 7 Schematic illustration. Possible mechanism of the CN–InO/GdF photocatalyst.

CN–InO cannot be utilized for the oxidation of $^{-}$OH to $^{\bullet}$OH (+1.99 eV *vs* NHE), whereas electrons in the CB of $GdFeO_3$ could not react with O_2 to form $^{\bullet}O_2^{-}$ (−0.33 eV *vs* NHE) for the reduction because of their standard redox potentials. Therefore, the conjectured type-II mechanism is not a reliable path for charge transfer and thermodynamical detriment for the degradation process[52]. For the Z-scheme route, the CB edge of CN–InO was more negative than the standard redox potential and was able to generate effective $^{\bullet}O_2^{-}$. Similarly, the photogenerated hole in the VB of $GdFeO_3$ could oxidize $^{-}$OH to produce $^{\bullet}$OH *via* appropriate energy levels. Upon light irradiation, the electrons generated in the CB of $GdFeO_3$ recombined with the holes in the VB of CN–InO. Hence, the remaining electrons in the CB of CN–InO and holes in the VB of $GdFeO_3$ could react with O_2 and $H_2O/^{-}OH$, respectively[53]. The produced active radical species could jointly promote the photocatalytic removal of TC, and the intermediates of TC converted into less toxic small molecules. Thus, the experimental facts confirmed that the CN–InO/GdF heterojunction facilitated a Z-scheme charge transfer and greatly enhanced redox performance.

From the frontier orbital theory, the vulnerable atomic sites of TC were determined using the highest occupied molecular orbital (HOMO) and the least unoccupied molecular orbital (LUMO) *via* conceptual density functional theory (DFT) calculations (Gaussian 09 and Gauss View 06 program), and the respective values are displayed in Fig. 8a–c. The HOMOs were located in the C15, C19, C21, C23, C28, C27, N9, O1, O4, O5, O6, and O8 atoms, whereas the LUMOs were localized around C11–C15, C17–C24, C26, C28–32, N9–10, O1, O3–6, and O8 atoms. These indicated that the above atomic sites were attacked by the radicals produced by the CN–InO/GdF nanocomposites. Additionally, in Fig. 8d, the electrostatic potentials (ESPs) with surface maxima and minima values were plotted, exhibiting the distribution of molecular charges over the TC[54]. For validating the degradation products from ultra-high-performance liquid chromatography–mass spectrometry (LC–MS) analysis, the Fukui indices were employed to determine whether the reactive active sites were attacked by one of the following factors: electrophilic (f^{-}), nucleophilic (f^{+}), and free radicals attack (f^{0}). The calculated Hirshfeld charges and condensed Fukui functions[55] are mentioned in Supplementary Table 3. Normally, the higher the Fukui values (f^{+}, f^{-}, and f^{0}), the greater the chances for $^{\bullet}O_2^{-}$, $^{\bullet}$OH, and h^{+} attack. However, the f^{-} values were dominant in N9 ($f^{-} = 0.1343$), O8 ($f^{-} = 0.0474$), and C27 ($f^{-} = 0.0285$) of TC, which clearly indicated that the atomic sites were strongly attacked by nucleophilic species ($^{\bullet}O_2^{-}$). Meanwhile, the f^{+} values in atoms like C18 ($f^{+} = 0.0822$), O3 ($f^{+} = 0.0725$), and N10 ($f^{+} = 0.0112$) showed significant threats from electrophilic species (h^{+}). Thus, free radical attack ($^{\bullet}$OH) occurred on the N9 ($f^{0} = 0.0658$) and O3 ($f^{0} = 0.0495$) atoms, respectively[56,57].

According to the outcomes gained from the above Fukui functions and DFT calculations, the possible degradation pathways of TC (Fig. 8e) and their anticipated fragmentation products were proposed in accordance with the mass/charge values at different times (initial, 30 min and 60 min) in Supplementary Fig. 9. Therefore, 12 fragmented patterns with subsequent chemical structures are identified and summarized in Supplementary Table 4. The overall pathway represented the breakdown of a series of active sites, such as deamination, demethylation, dealkylation, dehydroxylation, and ring cleavages, into tiny, mineralized byproducts. In pathway I, the hydroxyl group (OH) was bonded with the TC molecule to form IP1 ($m/z = 461$). In pathways II and III, the active sites from intense f^{-} values, such as N-dimethyl amino and methyl moieties, underwent a breakdown process in the development of two intermediate products, IP2 ($m/z = 431$) and IP3 ($m/z = 417$), respectively. This was followed by higher f^{-} and f^{+} values originating in the dehydroxylation and deamination of IP4 ($m/z = 402$) toward the formation of IP5 ($m/z = 387$) and IP7 ($m/z = 329$). Meanwhile, IP2 was broken into IP6 ($m/z = 358$) through deamidation and dehydroxylation. Additionally, the fragmented products were cut down into IP8 ($m/z = 312$) *via* deamination, demethylation, and dehydroxylation. Then, the dissociation emerged at the ring opening sites of the fused four rings of atoms because of the higher f^{+} and f^{0} values, which resulted in the generation of the unstable intermediate product

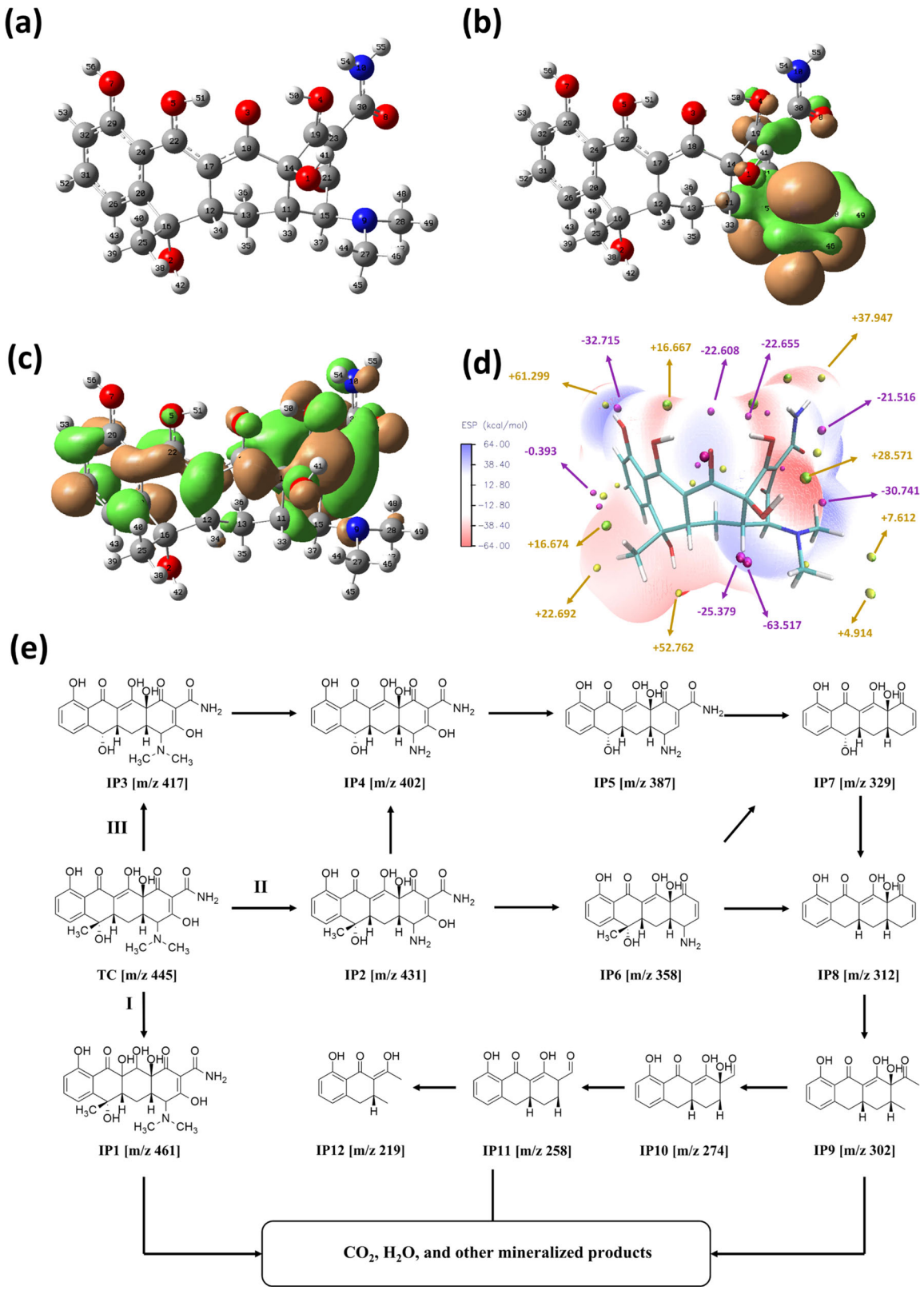

Fig. 8 Conceptual DFT calculation and degradation pathway. a Optimized TC structure with corresponding atomic labels. **b** HOMO and (**c**) LUMO orbitals using DFT calculation (gray, carbon; blue, nitrogen; red, oxygen; and white, hydrogen). **d** ESP potentials with surface charge distribution values (yellow, surface maxima; magenta, surface minima). **e** Proposed degradation pathway of TC and its intermediate products through visible light irradiation.

IP9 ($m/z = 302$). Later on, the intermediates were further oxidized by a series of reactions through demethylation, dehydroxylation, and minor ring opening sites in the formation of IP10 ($m/z = 274$), IP11 ($m/z = 258$), and IP12 ($m/z = 219$). This was followed by the complete mineralization of breakdown fragments into CO_2, H_2O, and other small molecular species[43]. Finally, the Fukui function and predicted degradation products further attested the scavenger test results by promoting a greater active radical role in the breakdown of TC.

As displayed in Fig. 9, the toxicity of TC and its degraded byproducts were evaluated using the ECOSAR 2.2 program with corresponding QSAR models. Additionally, in Supplementary Table 5, the major endpoints of lethal concentration (LC50) and lethal dosage concentration (LD50) for specific living organisms were estimated and summarized. Fig. 9a, b represents the computed chronic endpoints for fish (LD50), exhibiting a higher exposure of toxicity levels than that of the acute endpoints. Particularly, IP0–IP5 was limited in the toxic region ($1 < 10$ mg L^{-1}), followed by IP6–IP8 in less harmful levels. Meanwhile, in daphnia magna LC50 and LD50 (Fig. 9c, d), the major intermediates (IP1–5) and TC (IP0) relied on toxic regions with concentration levels of around 5.1–11 mg L^{-1} under short-term exposure; however, the concentration endpoints of chronic exposure were replicated in a more intense toxicity level (1.3–6.3 mg L^{-1}). From Fig. 9e, f, the acute and chronic toxicities of green algae (EC50) displayed an inhibition effect on algae growth (IP0–IP5), whereas the remaining concentrations endured in the harmful region. Therefore, TC and other initially mediated byproducts limited the toxic regions; however, subsequent degradation resulted in fewer harmful fragments (IP6–IP9). Finally, the Z-scheme CN–InO/GdF broke down the TC into less toxic fragments, which did not greatly impact the aquatic ecosystems.

In conclusion, a MOF-derived CN–InO hybrid with $GdFeO_3$ heterojunction catalysts was successfully prepared for the remarkably enhanced photocatalytic degradation of TC under visible light irradiation. The morphology, chemical structure, and optical properties of the CN–InO/GdF nanocomposites were systematically characterized by FESEM, HRTEM, BET, XRD, XPS, UV–Vis DRS, and PL spectra. The removal of TC in the presence of CN–InO/GdF-3 reached approximately 99.06% within 60 min of irradiation with a rate constant of 0.0536 min^{-1}, a value much higher than that of CN–InO (7.1) and $GdFeO_3$ (9.7). The formation of a direct Z-scheme CN–InO/GdF heterostructure not only effectively inhibited the recombination of electron–hole pairs but also enhanced the redox power. Meanwhile, C and N atoms improved the electron transfer in the CN–InO/GdF, which promoted the proliferation of rich reactive sites for surface reactions. Quenching tests and ESR analysis revealed the substantial role of ROS in TC degradation. Besides, the possible degradation pathway of TC was proposed based on DFT calculations and LC–MS analysis. This research affords a new understanding of the rational design of MOF-derived In_2O_3–based Z-scheme catalysts for a wide range of environmental applications.

METHODS

Catalyst preparation

Preparation of MIL-68 (In). First, 0.24 g of $C_8H_7NO_4$ and 0.6 g of $In(NO_3)_3{\cdot}xH_2O$ were dissolved in 20 mL of C_3H_7NO and stirred for 2.5 h to form a homogeneous solution. Then, the above mixture was switched to a 50-mL Teflon-lined autoclave at 125 °C for 5 h in an oven and cooled to natural temperature. The resulting yellow solids were washed with ethanol three times and finally dried at 80 °C under vacuum conditions.

Preparation of C, N-In_2O_3. The as-prepared MIL-68 (In) was ground in a mortar, transferred into an alumina boat, and tightly wrapped with aluminum foil paper to prevent it from floating. Subsequently, MIL-68 (In) was pyrolyzed in a tube furnace under a nitrogen (N_2) atmosphere with a heating rate of 5 °C min^{-1} for 2 h. The C, N-loaded In_2O_3 samples were prepared at different temperatures of 450 °C, 500 °C, and 550 °C. The corresponding catalysts were separately named CN–InO-450, CN–InO-500, and CN–InO-550. For comparison, MIL-68 (In) was also pyrolyzed in an oxygen (O_2) environment and denoted as S-In_2O_3.

Preparation of $GdFeO_3$. A simple hydrothermal approach was used to synthesize $GdFeO_3$ microspheres. Briefly, 2.25 g of $Gd(NO_3)_3{\cdot}6H_2O$ and 2.02 g of $Fe(NO_3)_3{\cdot}9H_2O$ were poured into 40 mL of H_2O under vigorous stirring to get a clear solution. After adding 1.92 g of $C_6H_8O_7{\cdot}H_2O$ and 10 mL of $C_2H_8O_2$, the yellow-colored mixture was stirred for another 30 min at 25 °C. The resultant solution was moved in a 100-mL stainless steel autoclave and heated in an oven at 180 °C for 12 h, naturally cooled, and collected through centrifugation. Afterward, the precipitate was washed several times with H_2O and $C_2H_8O_2$ and then dried. Finally, the resulting solid was annealed at 800 °C for 3 h in an ambient atmosphere.

Preparation of the C, N-In_2O_3/$GdFeO_3$ nanocomposites. The targeted C, N-In_2O_3/$GdFeO_3$ composites were prepared using a facile wet-chemical strategy. Typically, 1 g of as-fabricated C, N-In_2O_3 was ultrasonically dispersed in 50 mL of H_2O and stirred for 30 min. After continuous stirring, a certain amount of $GdFeO_3$ (x is the weight ratio of $GdFeO_3$ to C, N-In_2O_3) was added to the above system and then allowed to stir for 6 h. Lastly, the produced sample was washed and dried and then annealed at 300 °C in a tube furnace for 1 h under an N_2 atmosphere. Following the same protocol, C, N-In_2O_3/$GdFeO_3$ composites with various weight percent ratios of $GdFeO_3$ (C, N-In_2O_3/$GdFeO_3$ [1:0.25], C, N-In_2O_3/$GdFeO_3$ [1:0.5], C, N-In_2O_3/$GdFeO_3$ [1:0.75], and C, N-In_2O_3/$GdFeO_3$ [1:1]) were obtained and labeled as CN–InO/GdF-1, CN–InO/GdF-2, CN–InO/GdF-3, and CN–InO/GdF-4, respectively.

Photocatalytic measurement

The photocatalytic performances of the as-prepared samples were evaluated under visible light irradiation for the degradation of TC. The physiochemical properties of TC are tabulated in Supplementary Table 6. In detail, a 50-mL aqueous solution of TC (10 mg L^{-1}) was placed in a cylinder-shaped reactor, and 30 mg of catalyst (0.6 g L^{-1}) was added to the reactor. Before irradiation, the reaction mixture was stirred for 30 min in darkness to achieve an adsorption–desorption symmetry between the catalyst surface and TC. After this period, the reactor's content was irradiated using a 300-W xenon lamp with continuous stirring (DXP300s, DY Tech. Co., Republic of Korea) for 60 min. During the irradiation test, 1-mL aliquots were withdrawn from the reactor at predetermined time intervals and filtered through a polytetrafluoroethylene (pore size = 0.22 µm) syringe. The TC concentrations were monitored using high-performance liquid chromatography (HPLC, Waters Alliance 2695, Milford, USA) equipped with an ultraviolet–visible (UV–Vis) detector. The HPLC was coupled with a C18 column (Agilent Technologies, USA), and the temperature was set to 40°C. The mobile phase consisted of ultrapure water (eluent A, 0.1% formic acid) and acetonitrile (eluent B, volume ratio = 80:20) at a flow rate of 1 mL/min. The degradation efficacy and reaction rate were calculated using Eqs. (1) and (2), respectively.

$$\%\text{Removal} = \frac{C_0 - C_t}{C_0} \times 100\% \quad (1)$$

$$\ln\frac{C_t}{C_0} = -kt \quad (2)$$

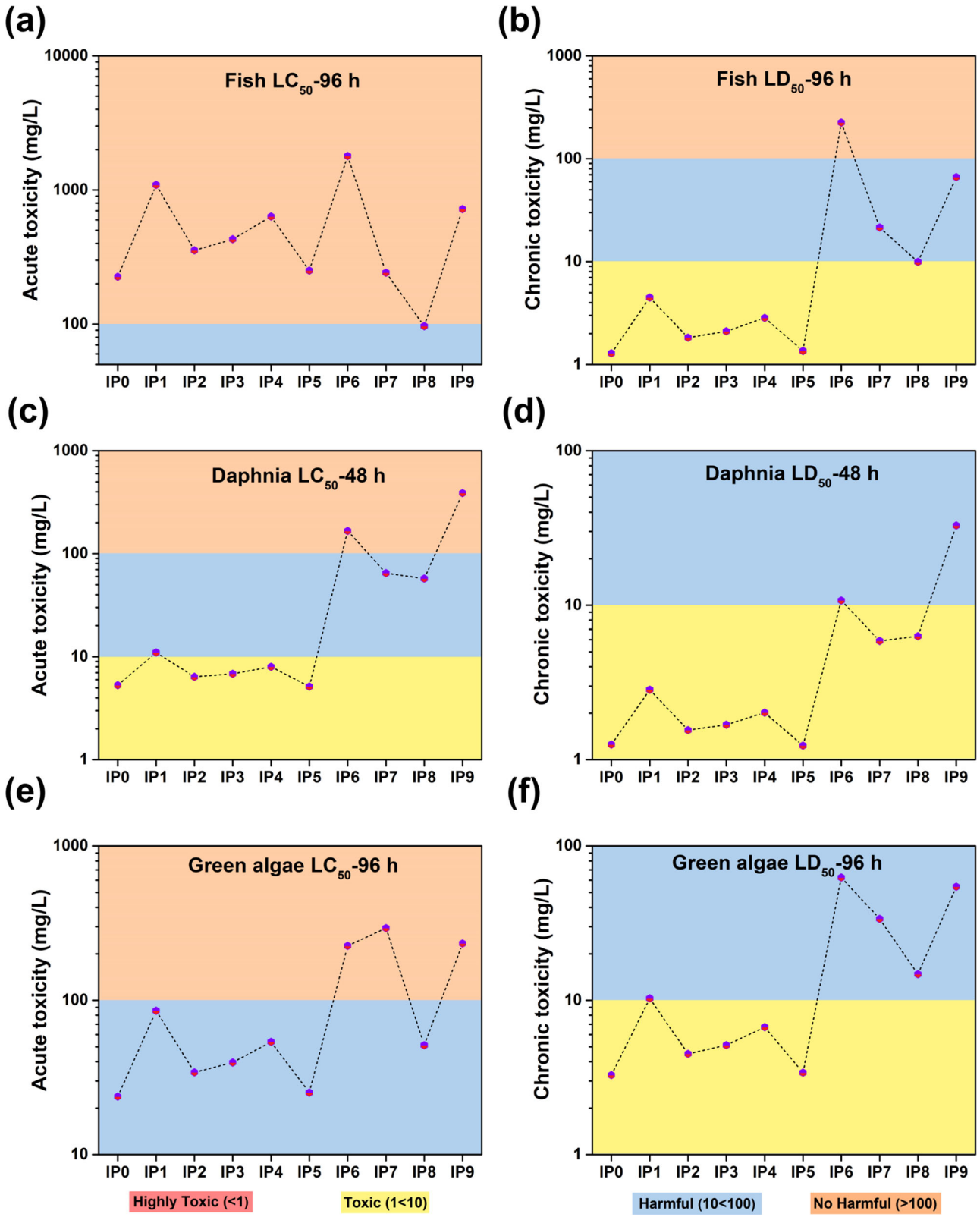

Fig. 9 Predicted acute (LC50) and chronic (LD50) toxic levels of TC and its intermediate byproducts using three living organisms. a, b Fish-96 h, **c, d** Daphnia magna-48 h, **e, f** green algae-96 h.

where C_0 is the initial concentration of the TC solution, and C_t is the final concentration (mg L^{-1}) after photocatalytic degradation. t and k denote the illumination time (min) and rate constant (min^{-1}), respectively.

DATA AVAILABILITY

The data that support the findings of this study are available from the corresponding author upon reasonable request.

Received: 18 June 2023; Accepted: 20 October 2023;
Published online: 01 November 2023

REFERENCES

1. Wang, X., Jia, J. & Wang, Y. Combination of photocatalysis with hydrodynamic cavitation for degradation of tetracycline. *Chem. Eng. J.* **315**, 274–282 (2017).
2. Vo, T. K. & Kim, J. Facile synthesis of magnetic framework composite $MgFe_2O_4$@UiO-66(Zr) and its applications in the adsorption–photocatalytic degradation of tetracycline. *Environ. Sci. Pollut. Res.* **28**, 68261–68275 (2021).
3. Lin, Z. et al. Change of tetracycline speciation and its impacts on tetracycline removal efficiency in vermicomposting with epigeic and endogeic earthworms. *Sci. Total Environ.* **881**, 163410 (2023).
4. Huo, B. et al. High efficiently piezocatalysis degradation of tetracycline by few-layered MoS_2/GDY: mechanism and toxicity evaluation. *Chem. Eng. J.* **436**, 135173 (2022).
5. Cao, H.-L. et al. Photocatalytic degradation of tetracycline antibiotics over CdS/nitrogen-doped–carbon composites derived from in situ carbonization of metal–organic frameworks. *ACS Sustain. Chem. Eng.* **7**, 10847–10854 (2019).
6. Nguyen, T. H. A., Quang, D. T., Tan, L. V. & Vo, T. K. Ultrasonic spray pyrolysis synthesis of TiO_2/Al_2O_3 microspheres with enhanced removal efficiency towards toxic industrial dyes. *RSC Adv.* **13**, 5859–5868 (2023).
7. Abd El-Monaem, E. M. et al. A comprehensive review on LDH-based catalysts to activate persulfates for the degradation of organic pollutants. *npj Clean Water* **6**, 34 (2023).
8. Saravanakumar, K., Ramjan, M. M., Suresh, P. & Muthuraj, V. Fabrication of highly efficient visible light driven Ag/CeO_2 photocatalyst for degradation of organic pollutants. *J. Alloy. Compd.* **664**, 149–160 (2016).
9. Peng, X., Urso, M. & Pumera, M. Metal oxide single-component light-powered micromotors for photocatalytic degradation of nitroaromatic pollutants. *npj Clean. Water* **6**, 21 (2023).
10. Tan, M. et al. MOFs-derived plum-blossom-like junction In/In_2O_3@C as an efficient nitrogen fixation photocatalyst: Insight into the active site of the In^{3+} around oxygen vacancy. *J. Colloid Interface Sci.* **638**, 263–273 (2023).
11. Sun, L. et al. Double-shelled hollow rods assembled from nitrogen/sulfur-codoped carbon coated indium oxide nanoparticles as excellent photocatalysts. *Nat. Commun.* **10**, 2270 (2019).
12. Pawar, K. K. et al. In_2O_3 nanocapsules for rapid photodegradation of crystal violet dye under sunlight. *J. Colloid Interface Sci.* **561**, 287–297 (2020).
13. Dai, Y.-M., Lee, W.-lW., Lin, W.-C. & Chen, C.-C. Synthesis and photocatalytic properties of nano-crystalline In_2O_3. *J. Chin. Chem. Soc.* **60**, 1415–1424 (2013).
14. Wang, X. et al. Photothermal synergistic catalytic oxidation of ethyl acetate over MOFs-derived mesoporous N-TiO_2 supported Pd catalysts. *Appl. Catal. B: Environ.* **322**, 122075 (2023).
15. Vo, T. K., Nguyen, M. T., Nguyen, V. C. & Kim, J. Microwave-assisted synthesis of $MgFe_2O_4$-decorated UiO-66(Zr)-NH_2 composites for collaborative adsorption and photocatalytic degradation of tetracycline. *Korean J. Chem. Eng.* **39**, 2532–2541 (2022).
16. Li, X. et al. Micro/macrostructure and multicomponent design of catalysts by MOF-derived strategy: opportunities for the application of nanomaterials-based advanced oxidation processes in wastewater treatment. *Sci. Total Environ.* **804**, 150096 (2022).
17. Li, F. et al. Efficient photo-Fenton reaction for tetracycline and antibiotic resistant bacteria removal using hollow Fe-doped In2O3 nanotubes: From theoretical research to practical application. *Water Res.* **240**, 120088 (2023).
18. Xiao, W. et al. Functional metal/carbon composites derived from metal–organic frameworks: insight into structures, properties, performances, and mechanisms. *ACS Catal.* **13**, 1759–1790 (2023).
19. Behera, P. et al. ZIF-8 derived porous C, N co-doped ZnO modified B-g-C_3N_4: A Z-Scheme charge dynamics approach operative towards photocatalytic hydrogen evolution and ciprofloxacin degradation. *J. Photochem. Photobiol. A* **436**, 114415 (2023).
20. Zhang, Q. et al. In–N–In sites boosting interfacial charge transfer in carbon-coated hollow tubular $In_2O_3/ZnIn_2S_4$ heterostructure derived from In-MOF for enhanced photocatalytic hydrogen evolution. *ACS Catal.* **11**, 6276–6289 (2021).
21. Xu, M., Zhao, X., Jiang, H., Chen, S. & Huo, P. MOFs-derived C-In_2O_3/g-C_3N_4 heterojunction for enhanced photoreduction CO_2. *J. Environ. Chem. Eng.* **9**, 106469 (2021).
22. Wang, X. et al. Bottom-up strategy for precisely designing and fabricating direct Z-scheme photocatalyst with wedge-type heterointerface bridged by chemical bond. *Chem. Eng. J.* **445**, 136785 (2022).
23. Mandal, S., Adhikari, S., Choi, S., Lee, Y. & Kim, D.-H. Fabrication of a novel Z-scheme Bi_2MoO_6/GQDs/MoS_2 hierarchical nanocomposite for the photo-oxidation of ofloxacin and photoreduction of Cr(VI) as aqueous pollutants. *Chem. Eng. J.* **444**, 136609 (2022).
24. Chen, X. et al. A plasmonic Z-scheme Ag@AgCl/PDI photocatalyst for the efficient elimination of organic pollutants, antibiotic resistant bacteria and antibiotic resistance genes. *Appl. Catal., B* **324**, 122220 (2023).
25. Mahmoudi, F. et al. Application of perovskite oxides and their composites for degrading organic pollutants from wastewater using advanced oxidation processes: Review of the recent progress. *J. Hazard. Mater.* **436**, 129074 (2022).
26. Yun, K. et al. Fabrication of highly effective $Ag_6Si_2O_7/SmFeO_3$ heterojunction with synergistically enhanced sonophotocatalytic degradation of ciprofloxacin and production of H_2O_2: Influencing factors and degradation mechanism. *Chem. Eng. J.* **468**, 143491 (2023).
27. Ujwal, M. P., Yashas, S. R. & Shivaraju, H. P. & Kumara Swamy, N. Gadolinium ortho-ferrite interfaced polyaniline: Bi-functional catalyst for electrochemical detection and photocatalytic degradation of acetaminophen. *Surf. Interfaces* **30**, 101878 (2022).
28. Mohassel, R., Shabani-Nooshabadi, M. & Salavati-Niasari, M. Effect of g-C_3N_4 amount on green synthesized $GdFeO_3$/g-C_3N_4 nanocomposites as promising compounds for solid-state hydrogen storage. *Int. J. Hydrog. Energy* **48**, 6586–6596 (2023).
29. Li, L. et al. Step-scheme $GdFeO_3$/g-C_3N_4 heterostructures with outstanding photocatalytic activity. *J. Mater. Sci.: Mater. Electron.* **32**, 16400–16410 (2021).
30. Baeissa, E. S. Environmental remediation of aqueous methyl orange dye solution via photocatalytic oxidation using $AgGdFeO_3$ nanoparticles. *J. Alloy. Compd.* **678**, 267–272 (2016).
31. Jeong, J. S., Kim, Y. H. & Lee, J. Morphology and structure of nano-sized In_2O_3 crystals synthesized by wet reaction. *J. Korean Phys. Soc.* **42**, S254–S257 (2003).
32. Sun, Q. et al. Tuning photoactive MIL-68(In) by functionalized ligands for boosting visible-light nitrogen fixation. *ACS Appl. Mater. Interfaces* **14**, 53904–53915 (2022).
33. Liang, Q. et al. Converting organic wastewater into CO Using MOFs-derived Co/In_2O_3 double-shell photocatalyst. *ACS Appl. Mater. Interfaces* **13**, 40754–40765 (2021).
34. Sun, C., Hu, J., Wu, L., Xia, Q. & Jiao, F. Construction of a novel visible-light-driven Z-scheme NiAl-LDH modified $(BiO)_2CO_3$ heterostructure for enhanced photocatalytic degradation antibiotics performance in natural water bodies. *Ind. Eng. Chem. Res.* **62**, 466–477 (2023).
35. Adhikari, S., Lee, H. H. & Kim, D.-H. Efficient visible-light induced electron-transfer in z-scheme $MoO_3/Ag/C_3N_4$ for excellent photocatalytic removal of antibiotics of both ofloxacin and tetracycline. *Chem. Eng. J.* **391**, 123504 (2020).
36. Zhang, C. et al. Molecular engineering of donor-acceptor structured g-C_3N_4 for superior photocatalytic oxytetracycline degradation. *Chem. Eng. J.* **448**, 137370 (2022).
37. Adhikari, S., Mandal, S. & Kim, D.-H. 1D/2D constructed $Bi_2S_3/Bi_2O_2CO_3$ direct Z-Scheme heterojunction: A versatile photocatalytic material for boosted photodegradation, photoreduction and photoelectrochemical detection of water-based contaminants. *J. Hazard. Mater.* **418**, 126263 (2021).
38. Chen, R. et al. Enwrapping g-C_3N_4 on In_2O_3 hollow hexagonal tubular for photocatalytic CO_2 conversion: Construction, characterization, and Z-scheme mechanism insight. *J. Colloid Interface Sci.* **631**, 122–132 (2023).
39. Jagan, G., Saravanakumar, K., Li, J., Yoon, Y. & Park, C. M. Novel double Z-scheme g-$C_3N_5/BiFeO_3/ZnIn_2S_4$ heterojunction system with enhanced visible-light-induced photo-Fenton activity towards sulfamethoxazole degradation. *Chem. Eng. J.* **471**, 144707 (2023).
40. Guo, X., Duan, J., Wang, W. & Zhang, Z. Modified graphitic carbon nitride as the photocatalyst for wastewater treatment under visible light irradiation. *Fuel* **280**, 118544 (2020).
41. Duc, H. V. et al. Synthesis, characterization, and photocatalytic activity of multi-component $CdMoO_4$/g-C_3N_4/GO composite. *Environ. Eng. Res.* **28**, 220649–220640 (2023).
42. Saravanakumar, K. & Park, C. M. Rational design of a novel $LaFeO_3$/g-$C_3N_4/BiFeO_3$ double Z-scheme structure: Photocatalytic performance for antibiotic degradation and mechanistic insight. *Chem. Eng. J.* **423**, 130076 (2021).
43. Saravanakumar, K. et al. 2D/2D nitrogen-rich graphitic carbon nitride coupled Bi_2WO_6 S-scheme heterojunction for boosting photodegradation of tetracycline: Influencing factors, intermediates, and insights into the mechanism. *Compos. Part B* **234**, 109726 (2022).
44. Hu, J. et al. Halogen doped g-C_3N_4/ZnAl-LDH hybrid as a Z-scheme photocatalyst for efficient degradation for tetracycline in seawater. *Sep. Purif. Technol.* **309**, 123047 (2023).
45. Liang, Q. et al. Replacing Ru complex with carbon dots over MOF-derived Co_3O_4/In_2O_3 catalyst for efficient solar-driven CO_2 reduction. *J. Mater. Chem. A* **10**, 4279–4287 (2022).
46. Gordanshekan, A. & Arabian, S. Solaimany Nazar, A. R., Farhadian, M. & Tangestaninejad, S. A comprehensive comparison of green Bi_2WO_6/g-C_3N_4 and Bi_2WO_6/

TiO_2 S-scheme heterojunctions for photocatalytic adsorption/degradation of Cefixime: artificial neural network, degradation pathway, and toxicity estimation. *Chem. Eng. J.* **451**, 139067 (2023).
47. Deng, Y. et al. Unveiling the origin of high-efficiency charge transport effect of C_3N_5/C_3N_4 homojunction for activating peroxymonosulfate to degrade atrazine under visible light. *Chem. Eng. J.* **457**, 141261 (2023).
48. Ming, H. et al. Photocatalytic activation of peroxymonosulfate by carbon quantum dots functionalized carbon nitride for efficient degradation of bisphenol A under visible-light irradiation. *Chem. Eng. J.* **424**, 130296 (2021).
49. Annamalai, S. & Shin, W. S. In-situ pyrolysis of Undaria pinnatifida as a green carbo-catalyst for degradation of organic contaminants: role of inherent N and P in the degradation pathway. *Chem. Eng. J.* **465**, 142813 (2023).
50. Ren, H. et al. Chemically bonded carbon quantum dots/Bi_2WO_6 S-scheme heterojunction for boosted photocatalytic antibiotic degradation: Interfacial engineering and mechanism insight. *Appl. Catal., B* **330**, 122587 (2023).
51. Saravanakumar, K. et al. Construction of novel In_2S_3/Ti_3C_2 MXene quantum dots/$SmFeO_3$ Z-scheme heterojunctions for efficient photocatalytic removal of sulfamethoxazole and 4-chlorophenol: Degradation pathways and mechanism insights. *Chem. Eng. J.* **451**, 138933 (2023).
52. Dung Nguyen, M. et al. Z-scheme S, B co-doped g-C_3N_4 nanotube@MnO_2 heterojunction with visible-light-responsive for enhanced photodegradation of diclofenac by peroxymonosulfate activation. *Chem. Eng. J.* **452**, 139249 (2023).
53. Zhou, S. et al. Ultrahigh-performance visible-light photodegradation enabled by direct Z-scheme AgI/(Na,F)–C_3N_4 composites. *Compos., Part B* **224**, 109200 (2021).
54. Zhang, J. & Lu, T. Efficient evaluation of electrostatic potential with computerized optimized code. *Phys. Chem. Chem. Phys.* **23**, 20323–20328 (2021).
55. Lu, T. & Chen, F. Multiwfn: A multifunctional wavefunction analyzer. *J. Comput. Chem.* **33**, 580–592 (2012).
56. De Vleeschouwer, F., Van Speybroeck, V., Waroquier, M., Geerlings, P. & De Proft, F. Electrophilicity and nucleophilicity index for radicals. *Org. Lett.* **9**, 2721–2724 (2007).
57. Dong, Y. et al. Construction of a 0D/3D AgI/MOF-808 photocatalyst with a one-photon excitation pathway for enhancing the degradation of tetracycline hydrochloride: Mechanism, degradation pathway and DFT calculations. *Chem. Eng. J.* **460**, 141842 (2023).

ACKNOWLEDGEMENTS

This work was supported by the Basic Science Research Program through the National Research Foundation (NRF) of Korea funded by the Ministry of Education (NRF-2018R1A6A1A03024962) and the Korea government (MSIT) (No. 2021R1A2C2003734). The authors would also like to thank the Korea Basic Science Institute (Daegu) for FE-SEM measurements.

AUTHOR CONTRIBUTIONS

K.S.: conceptualization, methodology, software, visualization, calculation, writing—original draft. G.J.: methodology, software, validation, visualization. J.L.: Supervision; Validation; Visualization. C.M.P.: conceptualization, writing—review & editing, supervision, funding acquisition, validation, formal analysis.

COMPETING INTERESTS

The authors declare no competing interests.

ADDITIONAL INFORMATION

Supplementary information The online version contains supplementary material available at https://doi.org/10.1038/s41545-023-00288-0.

Correspondence and requests for materials should be addressed to Chang Min Park.

Reprints and permission information is available at http://www.nature.com/reprints

Publisher's note Springer Nature remains neutral with regard to jurisdictional claims in published maps and institutional affiliations.